2018

A transverse-Wakefield streaking technique for measurement of ultra-fast electron pulses

Jinlong Wang

ABSTRACT

A TRANSVERSE-WAKEFIELD STREAKING TECHNIQUE FOR MEASUREMENT OF ULTRA-FAST ELECTRON PULSES

Jinlong Wang, M.S.
Department of Physics
Northern Illinois University, 2018
Philippe Piot, Director

The development of future free electron lasers (FELs) requires reliable time-resolved measurements of ultra-short (less than ps) electron bunches, especially their temporal distribution. A possible technique is to streak the bunch in the transverse direction by means of time-dependent external electromagnetic fields. A passive deflector, consisting of a dielectric-lined waveguide, is used to produce electromagnetic wakefield that imparts a time-dependent transverse kick to a relativistic electron bunch that propagates off-axis. The present work explores the possible use of the self-generated electromagnetic fields.

NORTHERN ILLINOIS UNIVERSITY
DE KALB, ILLINOIS

AUGUST 2018

A TRANSVERSE-WAKEFIELD STREAKING TECHNIQUE FOR MEASUREMENT OF ULTRA-FAST ELECTRON PULSES

BY

JINLONG WANG

A THESIS SUBMITTED TO THE GRADUATE SCHOOL

IN PARTIAL FULFILLMENT OF THE REQUIREMENTS

FOR THE DEGREE

MASTER OF SCIENCE

DEPARTMENT OF PHYSICS

Thesis Director:
Philippe Piot

ACKNOWLEDGEMENTS

I first would like to thank my dear Professor Philippe Piot, without whom the thesis would not be possible. I would like to thank him for his patience and kindness, the support and guidance. I could not have imagined having a better advisor and mentor for my study in this university.

Besides my advisor, I would like to thank the rest of my thesis committee: Prof. Yasuo Ito and Prof. Dennis E. Brown, for their valued time and encouragement.

My sincere thanks also goes to Greg Fagerberg and Carlos Garcia, who gave access to the laboratory and research facilities and who helped me through the process. Without their support it would not have been possible to conduct this research.

This work was supported by the US Department of Energy under contracts No. DE-SC0011831 with Northern Illinois University. My sincere thanks for the support.

DEDICATION

To all the friends

TABLE OF CONTENTS

LIST OF TABLES

Table Page

LIST OF FIGURES

Figure Page

CHAPTER 1

INTRODUCTION

Ultra-short electron bunches (i.e. with duration < 1 ps) have a wide range of scientific applications. These include the generation of electromagnetic radiation in free electron lasers (FEL) [1, 2, 3] and the probing of dynamical processes in condensed matter, chemistry, or biology[4] via ultra-fast electron diffraction [5]. Likewise, short electron bunches are used in support of high-energy physics, e.g. in e^+-e^- particle colliders to probe the fundamentals of matter and forces [6].

As electron bunches with decreasing duration are becoming increasingly available, the associated formation process along with its optimization is often complex [7] and require precise diagnostics. Moreover, in many experiments, details of the bunch structure play an important role in the analysis of the experiment, for example, in time-resolved measurements performed at X-ray FEL [8].

However, measuring the duration of short electron bunches presents significant challenges. Usually, to measure a given time event, one would rely on an even shorter event to "probe" the pulse one needs to measure. Electromagnetic fields associated to a picosecond-duration electron bunch have a duration at the picosecond level, and no electronic device can directly register such a short signal (state-of-the-art diodes have a response time > 50 ps). Thus, the development of alternative diagnostic techniques to measure the ultra-short electron bunch is necessary.

Diagnostic techniques often employed to measure sub-picosecond electron bunches can be categorized in two classes: the frequency domain and the time domain; see for example, Ref. [9] for a comprehensive discussion.

For the most part, frequency domain techniques are based on detecting some form of coherent radiation (CR) emitted by short bunches. The radiated power emitted at a frequency $f \equiv 2\pi\omega$ via a given electromagnetic process by an electron bunch composed of N electron is given by [9]

$$P(\omega) = P_{inc}(\omega)[N + N(N-1)f(\omega)] \tag{1.1}$$

where $P_{inc}(\omega)$ is the incoherent single-electron emission spectrum associated to the considered emission process, and $f(\omega)$ is the bunch form factor that describes the coherent enhancement of the emission. The function $f(\omega)$ can be written as the square of the Fourier transform of the normalized longitudinal distribution function $S(t)$:

$$f(\omega) = |\int_{-\infty}^{\infty} S(t)e^{2\pi i\omega/t}|^2 \tag{1.2}$$

Here $\int_{-\infty}^{\infty} S(t)dt = 1$, and $S(t)$ is related to the current profile $I(t)$ via $I(t) = QS(t)$ where $Q = N|e^-|$ is the total charge in the bunch. Note that Eq. 1.2 assumes the bunch to be a line charge distribution.

Thus, at a frequency where the radiation is coherent, i.e. $f(\omega) \sim \mathcal{O}(1)$, a measurement of $P(\omega)$ provides indirect information on $S(t)$ from the measurement of $f(\omega)$. The dependence of the power versus frequency can be measured with a spectrometer [10] or via an autocorrelation method [11]. In addition, several radiation mechanisms can be used including coherent synchrotron radiation (CSR), transition radiation (CTR) or diffraction radiation (CDR) [9]. The advantage of the CSR resides in its non-invasive character, but the incoherent spectrum changes as a function of wavelength, making it more difficult to analyze the measurement results. Instead, the CTR method has the advantage of relatively high power and a flat

incoherent emission spectrum. The principal disadvantage associated to CTR comes from its destructive nature (the bunch has to be intercepted with a thin metallic sheet), thereby making it unsuitable as a continuous bunch duration monitor [9].

All the frequency-domain methods have a fundamental limitation. The bunch distribution cannot be determined unambiguously, no matter whether it is an auto-correlation measurement or a spectrum measurement, because the phase information necessary to obtain the Fourier transform of the bunch distribution is lost in the measurement as only the radiation energy or power (related to the modulus of the electromagnetic field) can be detected.

Time-domain techniques directly measure a quantity that is proportional to the bunch current profile and rely on either directly measuring the temporal distribution of the Lorentz-boosted Coulomb field attached to an electron bunch or involve methods that map the time coordinate into one of the spatial coordinates.

An example of the former technique is the electro-optical imaging [12] where an electron bunch propagates very close to a birefringent crystal and the associated change in birefringence is probed with an ultra-short laser pulse. The Coulomb-field temporal distribution is then encoded on the optical laser spectrum which is measured via standard laser-characterization techniques [12].

The other type of time-domain methods regards techniques that map the temporal coordinate into a spatial ones. These techniques can be applied directly on the electron bunch or to the radiation field emitted by the electron bunch. In the latter case a streak camera [13] can be used to directly measure the duration of optical pulses emitted by the bunch (via processes similar to the ones discussed in the context of the time-domain method). The resolution of state-of-the-art streak camera can attain ~ 100 fs.

Examples where the time-to-space mapping is directly applied to the electron beam include the zero-phasing [14] and the deflecting-cavity [15] techniques. In the zero-phasing measurement [14], a radiofrequency (RF) linear accelerator is phased to the zero crossing of the accelerating wave so as to introduce a linear time-energy correlation along the bunch. Sending the beam in a dispersive section (where each electron transverse offset is proportional to its energy) provides a distribution along the dispersive axis which is representative of the energy spectrum and therefore of the time distribution (since energy and time are linearly correlated). The beamline settings and detailed design of the dispersive section can be used to calibrate the measurement and obtain an absolute current distribution.

The deflecting-cavity measurement had recently become very popular in large FEL-user facilities. The idea of using an RF deflecting structure to kick the electron beam was first proposed in 1960s [16]. The RF transverse deflecting structure (TDS) provides a time-varying transverse deflecting field which induces a linear correlation between time and the transverse beam distribution. Therefore measuring the beam transverse distribution downstream of the TDS is representative, under certain assumptions, of the beam's current distribution. Unfortunately, the TDS technique is quite expensive (on the order of $1M$ dollars in 2018) for high-energy beams with ultra-short (sub-ps) bunch length. The cost is mainly driven by the auxiliary device (klystrons) needed to power the cavity. So far resolutions on the order of femtoseconds have been reported [8].

The present work explores a time-domain mapping method which employs self-generated electromagnetic fields to streak the bunch as recently proposed in Ref. [17]. This "passive streaking" technique is appealing owing to its simplicity (the beam just needs to be transported through a small dielectric capillary tube or corrugated waveguide), but its analysis is complicated as the introduced correlation between the temporal and spatial coordinates is nonlinear. In this thesis we explore the passive-streaking technique based on a dielectric-lined waveguide (DLW). We first discuss the transverse force imparted on a bunch as it

propagates off axis in a DLW and develop a program to compute the electromagnetic field excited by a bunch propagating in a DLW using the formalism presented in Ref. [18]. The code is used to simulate and investigate the proposed passive-streaking method. Finally an iterative algorithm to enable the reconstruction of the bunch temporal profile is presented and the performances of the streaking method is investigated.

CHAPTER 2

ELECTROMAGNETIC WAKEFIELD

A charged-particle beam with the speed of light interacts electromagnetically with its surroundings via fields radiated due to change in boundary condition. These fields are commonly referred to as electromagnetic wakefield or wakefield. In this chapter, we introduce wakefield along with the concept of wake potential. We derive the associated energy or transverse kick experienced by an electron-bunch distribution.

2.1 Interaction Between Moving Charged Particles

Charged particles uniformly moving in free space only interact via space-charge effect (arising from Coulomb repulsion). Interaction via radiative field can occur under various conditions. One of them is when the particles surrounding boundary changes (this is known as geometric wakefield). Another possible cause stems from the finite conductivity of the beam pipe used to enclose the beam to an ultra-high vacuum environment. This effect is referred to as resistive wakefield. In this section we follow Reference [19] and consider resistive effect to illustrate the impact of wakefield.

We start by considering a simple two-particle model moving uniformly in the beam pipe. Take the leading "source" particle of charge q moving with velocity v and a trailing "test" particle of unit charge moving behind the leading one on a parallel path at a axial distance s with an transverse offset x in free space as shown in Fig. 2.1.

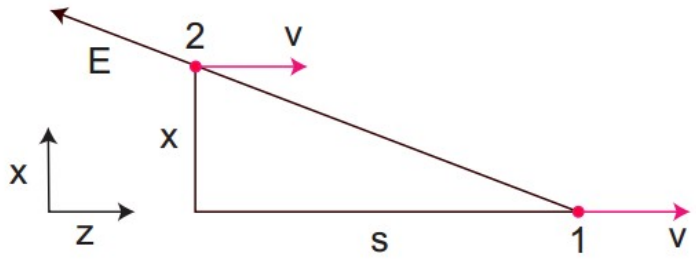

Figure 2.1: Leading particle 1 and trailing particle 2 traveling in free space with parallel velocity $\boldsymbol{v}$ (from Ref. [19]).

In order to find the force which the leading particle exerts on the trailing one, we first remind the electromagnetic field generated by the leading particle:

$$\begin{aligned} \mathbf{E} &= \frac{q\mathbf{R}}{\gamma^2 R^3}, \\ \mathbf{H} &= \frac{1}{c}\mathbf{v} \times \mathbf{E} \end{aligned} \tag{2.1}$$

Here $\mathbf{R}$ is the vector from point 1 to point 2, i.e. the distance separating the particle $R^2 = s^2 + x^2/\gamma^2$; see Fig. 2.1. The longitudinal force acting on the trailing unit charge is then given by $F_l \equiv 1\boldsymbol{E}.\hat{s}$:

$$F_l = E_z = -\frac{qs}{\gamma^2(x^2 + x^2/\gamma^2)^{3/2}} \tag{2.2}$$

and the transverse force acting on the trailing unit charge in the direction of x is [19]

$$F_t = E_x + \vec{v} \times \vec{B} = E_x - v/cB_y = \frac{qx}{\gamma^4(x^2 + x^2/\gamma^2)^{3/2}} \tag{2.3}$$

Here

$$\vec{v} = (0, 0, v), \vec{B} = (B_x, B_y, B_z)$$

$$E_x - v/cB_y = \frac{qx}{\gamma^2(x^2 + x^2/\gamma^2)^{3/2}} - \beta^2 \frac{qx}{\gamma^2(x^2 + x^2/\gamma^2)^{3/2}} = \frac{qx}{\gamma^4(x^2 + x^2/\gamma^2)^{3/2}}$$

The above interaction in free space is a Coulomb-type interaction mediated by the Lorentz-boosted Coulomb fields. We note that in the limit of ultra-relativistic particles, the longitudinal and transverse forces vanish as $\gamma \to \infty$. Hence, in the ultra-relativistic limit of uniformly moving, particles do not interact in free space.

In fact if the particles are traveling along the axis of a perfectly conducting cylindrical pipe, the same observation applies as the interaction with the perfect conductor can be modeled via an image-charge approach where all the charges move at the same velocity. Therefore even in the ultra-relativistic limit, the image charges won't generate any forces that would act back on the particles, no matter how close to the wall the particles are.

However, for a resistive wall where the image fields drag significant distances behind the charge or any sudden variation of the pipe cross section, would produce an electromagnetic force acting back on the particles. In Fig. 2.2, we can see the sudden change of the cross section of the pipe. The ultra-relativistic charged particles travel from left to right with contracted field lines spreading out only within an angle $\pm 1/\gamma$.

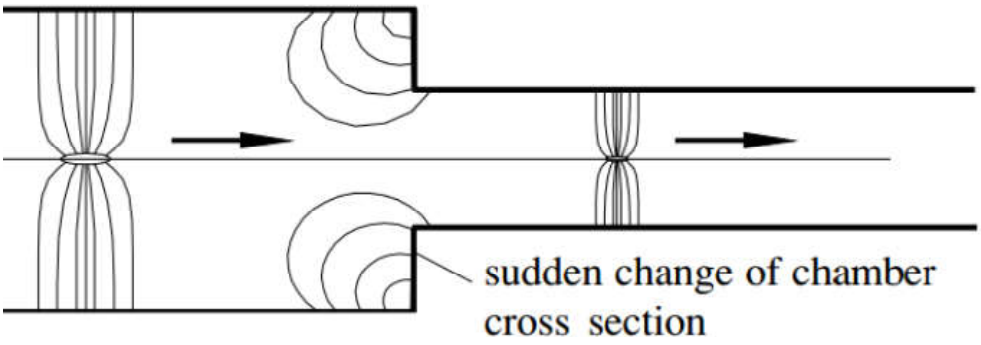

Figure 2.2: Obstacle on uniform vacuum chamber surface[20].

In this case, this resulting force can have the ability to pull or push the charge q or test particles following that charge, thus the wakefield is created. In the time domain, the interaction is described by wakefield which acts back on charges[20]. The energy losses of a single particle or collection of particles resulting from the wakefield can cause important modifications in the dynamics of particle motion.

2.2 Wake Function

Assume that we've already known the electromagnetic fields in a DLW structure by solving the Maxwell's equations. If a point charge q traverses this structure with offset

parallel to the z-axis at the speed of light, *wake function* [21] can be defined as integrals over the normalized forces due to the electromagnetic fields excited by the point charge q and evaluated at a distance s behind it:

$$w(\vec{\rho}_b, \vec{\rho}_e, s) = \frac{1}{q}\int_{-\infty}^{\infty} dz[\hat{E}(\vec{\rho}_b, \vec{\rho}_e, z, t = \frac{z+s}{c}) + c\hat{z} \times \hat{B}(\vec{\rho}_b, \vec{\rho}_e, z, t = \frac{z+s}{c})] \tag{2.4}$$

where $\vec{\rho}_b$ is the transverse offset of the test charge, $\vec{\rho}_e$ is the transverse offset of the exciting charge, and s is the distance at which the test charge travels behind the exciting charge along the traveling axis in the structure.

Specifically, we can introduce longitudinal wake function and transverse wake function according to the direction of the integrated components. If the charged particle travels at the ultra-relativistic constant velocity $v \sim c$, then the wake function ahead of the exciting particle vanishes when $s < 0$, where s is the axial distance from the leading particle to the test particle, since the electromagnetic fields cannot propagate ahead of particles when they move with the same speed of light. This is often referred to as *causality principle* [19].

2.2.1 Longitudinal Wake Function

The *longitudinal wake function* can be defined by integrating over the longitudinal component of the electric field E_z normalized by a test charge q which moves along a trajectory parallel to the axis of the dielectric-lined waveguide structure [21]:

$$w_l(\vec{\rho}_b, \vec{\rho}_e, s) = \frac{1}{q}\int_{-\infty}^{\infty} dz E_z(\vec{\rho}_b, \vec{\rho}_e, z, t = \frac{z+s}{c}) \tag{2.5}$$

where $\vec{\rho}_b$ is the transverse offset of the test charge, $\vec{\rho}_e$ is the transverse offset of the exciting charge, and s is the distance at which the test charge travels behind the exciting charge along the traveling axis in the structure.

We can decompose the longitudinal wake function as an expansion in azimuthal modes in structures with axial symmetry . Using cylindrical coordinates, we can get [21]

$$w_l(\rho_b, \rho_e, s, \theta) = \sum_{m=0}^{\infty} \rho_b^m \rho_e^m \cos m\theta w_l^m(s) \tag{2.6}$$

Here θ is the angle between the test charge and the exciting charge, i.e. $\theta = \angle(\vec{\rho}_b, \vec{\rho}_e)$

2.2.2 Transverse Wake Function

Also, assuming that we know the electromagnetic fields in the structure, the *transverse wake function* can be defined as the integral over the transverse electromagnetic forces along a straight path at a distance s behind an exciting ultra-relativistic charge normalized to the charge [22]

$$\vec{w_t}(\vec{\rho}_b, \vec{\rho}_e, s) = \frac{1}{q} \int_{-\infty}^{\infty} dz [\vec{E}(\vec{\rho}_b, \vec{\rho}_e, s, t = \frac{z+s}{c}) + \vec{v} \times \vec{B}(\vec{\rho}_b, \vec{\rho}_e, s, t = \frac{z+s}{c})]_{\perp} \tag{2.7}$$

For a structure with axial symmetry, using the cylindrical coordinates, the transverse wake function can be written as[22]:

$$\vec{w_t} = \sum_{m=1}^{\infty} \rho_b^{m-1} \rho_e^m (\hat{\rho} \cos m\theta - \hat{\theta} \sin m\theta) w_t^m(s) \tag{2.8}$$

If both particles have the same charge, then a positive transverse wake means that the trailing particle experiences a transverse **kick** in the direction along offset of the wakefield-exciting particle.

2.3 Wake Potential

So far we have defined wake functions which are associated to the force experience by the a trailing (or test) particle. These functions can be thought of as Green's function. The integrated effect on a particle distribution is described by the *wake potential*, which is defined as the integral over the electromagnetic forces exerted by wakefield at the position of a test charge following exciting charge on the same trajectory. The exciting charge is now a bunch of particles of finite length instead of one particle, and the distance ζ to the test charge is measured from the bunch center.

The *longitudinal wake potential*[23] for a bunch of charged particles can be found from the convolution of the longitudinal wake function with the normalized density $\Lambda(z)$:

$$W_l(z) = \int_{-\infty}^{z} d\zeta w_l(z-\zeta)\Lambda(\zeta) \tag{2.9}$$

As we can see, if the normalized density $\Lambda(z)$ is a δ function, the wake potential would reduce to the wake function itself. We can decompose an arbitrary distribution into an infinite series of orthogonal polynomials to determine longitudinal wake potentials numerically. The coefficients of polynomials can be obtained using the orthogonality of the expansion functions. But this method has a problem due to the limited accuracy because we have to do a truncation of the expansion at a relatively low order.

Similarly, when one assumes a constant displacement of the bunch from the axis, the transverse wake potential[23] can be written as

$$W_t(z) = \int_{-\infty}^{z} d\zeta w_t(z-\zeta)\Lambda(\zeta) \tag{2.10}$$

There exists a relation between the transverse wake potential and longitudinal potential. The relation between the longitudinal derivation of the transverse wake potential and the transverse gradient of the longitudinal potential is referred to as the Panofsky-Wenzel theorem. The gradient in the longitudinal and transverse directions of the wake potential can be obtained[19]:

$$w_l = \frac{\partial W}{\partial s}, w_t = \nabla_{\vec{\rho}} W \tag{2.11}$$

Note that $\nabla\vec{\rho} = \hat{x}\frac{\partial}{\partial x} + \hat{y}\frac{\partial}{\partial y}$ is a two-dimensional gradient with respect to coordinates x and y. From Eq. 2.11, we can also know that

$$\frac{\partial w_t}{\partial s} = \nabla_{\vec{\rho}} w_l \tag{2.12}$$

This relation above is usually referred to as the *Panofsky-Wenzel theorem.*

CHAPTER 3

WAKEFIELD IN A CYLINDRICAL SYMMETRIC DIELECTRIC-LINED WAVEGUIDE

In this chapter we derive the wakefield excited by a charged particle in a dielectric-lined waveguide (DLW). We consider a cylindrical metal tube of radius a. The tube is filled partially with isotropic material with uniform dielectric constant ϵ between radii $b < r < a$; see geometry in Fig. 3.1.

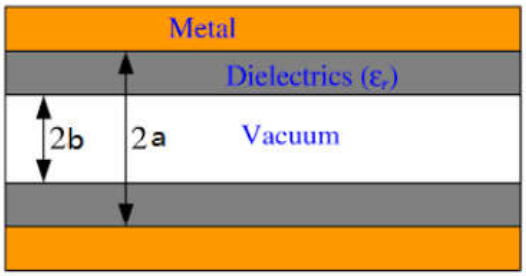

Figure 3.1: Basic structure of a dielectric-lined waveguides [24]. b is the inner radius, a is outer radius.

The dielectric-lined waveguides (DLW) consist of normal conducting waveguides with a thin dielectric liner on the interior surface; see Fig. 3.1. The DLW was initially introduced as a possible structure for beam-driven wakefield acceleration. In such a scheme the electromagnetic fields produced by the bunch were tailored to provide a high accelerating field [$\mathcal{O}$(GeV/m)] to accelerate a following electron bunch. However, the DLW structure has found other applications in an accelerator, including its possible use to shape an electron-bunch distribution [25].

Qualitatively the dielectric coating slows down the traveling electromagnetic wave exited by the beam. If the wave phase velocity is matched to the beam velocity a net energy exchange between the beam and wave can occur. DLWs can be shaped to follow any geometry; however, we will focus on the cylindrically symmetric DLW structure for sake of simplicity. In a cylindrical symmetric DLW, a hollow dielectric cylinder has its outer surface contacted to a conductor (typically a high-conductivity metal such as copper); see also Fig. 3.1. Our derivation closely follows the seminal work by Ng [18] and the derivation provides the basis for the development of an algorithm used to numerically compute the wakefield and wake potentials.

3.1 Derivation of Wakefield

3.1.1 Longitudinal Field

Consider the source particle of charge q travels with velocity of $\boldsymbol{v} = \beta c\hat{\boldsymbol{z}}$ along the cylindrical waveguide at an offset r_0 from the DLW axis; the Maxwell's equations written in CGS units for the longitudinal fields take the form [18]

$$(\nabla^2 - \frac{\mu\epsilon}{c^2}\frac{\partial^2}{\partial t^2})E_z = \frac{4\pi}{\epsilon}\frac{\partial \rho}{\partial z} + \frac{4\pi\mu}{c^2}\frac{\partial J_z}{\partial t} \tag{3.1}$$

$$(\nabla^2 - \frac{\mu\epsilon}{c^2}\frac{\partial^2}{\partial t^2})B_z = 0 \tag{3.2}$$

Here the charge density and current density about quantities (r, θ, z, t) are

$$\rho(r, \theta, z, t) = q\frac{\delta(r - r_0)}{r}\delta(\theta)\delta(z - vt), \text{and } J_z = v\rho \tag{3.3}$$

We can solve these equations in the Fourier domain by decomposing the field using

$$E_z(r, \theta, z, t) = \sum_{m=-\infty}^{\infty} e^{im\theta}\int_{-\infty}^{\infty} d\omega e^{i(z-vt)\omega/v}\tilde{E}_{zm}(r, \omega) \tag{3.4}$$

Considering the Dirac-function Fourier transformation

$$\delta(z - vt) = \frac{1}{2\pi v}\int_{-\infty}^{\infty} d\omega e^{i(z-vt)\omega/v} \tag{3.5}$$

and azimuthal decomposition

$$\frac{\delta(r-r_0)}{r}\delta(\theta) = \frac{1}{2\pi}\sum_{m=-\infty}^{\infty} e^{im\theta}\int_0^\infty kdkJ_m(kr)J_m(kr_0) \tag{3.6}$$

where J_m is the Bessel function of order m; the Eq. 3.1 can be written as

$$(\nabla^2 + \frac{\mu\epsilon\omega^2}{c^2})\tilde{E}_{zm}(r,\omega) = \tilde{\phi}_m(r,w) \tag{3.7}$$

where

$$\tilde{\phi}_m(r,w) = \frac{i4\pi\omega}{v\epsilon}(\tilde{\rho}_m - \frac{\mu\epsilon v}{c^2}\tilde{J}_m) = \frac{iq\omega(1-\mu\epsilon\beta^2)}{\pi v^2\epsilon}\int_0^\infty kdkJ_m(kr)J_m(kr_0) \tag{3.8}$$

For a particular solution, we can get

$$\tilde{E}_{zm}^{part} = -\frac{iq\omega}{\pi v^2\gamma^2}\int_0^\infty dk\frac{kJ_m(kr)J_m(kr_0)}{k^2+(\omega/v\gamma)^2}, 0<r<b \tag{3.9}$$

The integration over k is [18]

$$\tilde{E}_{zm}^{part} = \frac{-iq\omega}{\pi v^2\gamma^2}\begin{cases} I_m(\omega r/v\gamma)K_m(\omega r_0/v\gamma) & 0\le r\le b\ , \\ K_m(\omega r/v\gamma)I_m(\omega r_0/v\gamma) & b\le r\le a\ . \end{cases} \tag{3.10}$$

Here I_m and K_m are modified Bessel function and Hankel function. The relation between them is [26]

$$K_\alpha = J_\alpha \pm iY_\alpha, I_\alpha(x) = i^{-\alpha}J_\alpha(ix)$$

The general solution can be written as [18]

$$\tilde{E}_{zm}^{gen} = \begin{cases} \varepsilon_m I_m(kr_0) I_m(kr) & 0 \le r \le b \ , \\ A_m[J_m(sa)Y_m(sr) - Y_m(sa)J_m(sr)] & b \le r \le a \end{cases} \tag{3.11}$$

where $k = \frac{\omega}{v}\sqrt{1-\beta^2}, s = \frac{\omega}{v}\sqrt{\mu\epsilon\beta^2 - 1}$, and Y_m is the Neumann function of order m. Also, we can use the same method to get the general solution for $\tilde{B}_{zm}^{gen}$:

$$\tilde{B}_{zm}^{gen} = \begin{cases} B_m I_m(kr_0) I_m(kr) & 0 \le r \le b \ , \\ C_m[J'_m(sa)Y_m(sr) - Y'_m(sa)J_m(sr)] & b \le r \le a \end{cases} \tag{3.12}$$

The four constants ε_m, B_m, A_m, C_m can be determined by the matching condition at the boundary $r = b$ defining the interface between vacuum and the dielectric liner. At $r = b$, we have

$$\begin{aligned} &\tilde{E}_{zm}^{v} = \varepsilon'_m I_m + \eta'_m K_m, \tilde{E}_{zm}^{d} = A_m p_m \\ &\tilde{B}_{zm}^{v} = B'_m I_m, \tilde{B}_{zm}^{d} = C_m r_m \end{aligned} \tag{3.13}$$

where the abbreviated notations are defined as

$$\begin{aligned} &I_m = I_m(kb), K_m = K_m(kb) \\ &p_m = J_m(sa)Y_m(sb) - Y_m(sa)J_m(sb), r_m = J'_m(sa)Y_m(sb) - Y'_m(sa)J_m(sb) \\ &\eta'_m = \eta\frac{I_m(kr_0)}{\gamma^2}, \eta = -\frac{iq\omega}{\pi v^2} \\ &\epsilon'_m = \epsilon_m I_m(kr_0), B'_m = B_m I_m(kr_0) \end{aligned} \tag{3.14}$$

3.1.2 Transverse Field

Through the relation between the transverse electric fields E_t, magnetic flux density B_t and longitudinal fields [18]:

$$(\nabla_z^2 - \frac{\mu\epsilon}{c^2}\frac{\partial^2}{\partial t^2})\mathbf{B}_t = -\frac{i\omega\mu\epsilon}{c}\nabla_t \times \hat{z}\mathbf{E}_z + \nabla_t\nabla_z\mathbf{B}_z, \tag{3.15}$$

$$(\nabla_z^2 - \frac{\mu\epsilon}{c^2}\frac{\partial^2}{\partial t^2})\mathbf{E}_t = \frac{i\omega}{c}\nabla_t \times \hat{z}\mathbf{B}_z + \nabla_t\nabla_z\mathbf{E}_z \tag{3.16}$$

and knowing the E_z and B_z, the transverse electric field can be obtained [18] at the boundary $r = b$:

$$\begin{aligned}
\tilde{E}^v_{\theta m} &= \tfrac{iv\beta k}{\omega(1-\beta^2)}B'_m I'_m + \tfrac{mv}{\omega b(1-\beta^2)}(\varepsilon'_m I_m + \eta'_m K_m),\\
\tilde{E}^d_{\theta m} &= -\tfrac{iv\beta s}{\omega(\mu\epsilon\beta^2-1)}C_m r'_m - \tfrac{mv}{\omega b(\mu\epsilon\beta^2-1)}A_m p_m,\\
\tilde{E}^v_{rm} &= \tfrac{mv\beta}{\omega b(1-\beta^2)}B'_m I_m - \tfrac{ivk}{\omega(1-\beta^2)}(\varepsilon'_m I'_m + \eta'_m K'_m),\\
\tilde{E}^d_{rm} &= -\tfrac{mv\beta}{\omega b(\mu\epsilon\beta^2-1)}C_m r_m + \tfrac{ivs}{\omega(\mu\epsilon\beta^2-1)}A_m p'_m
\end{aligned} \tag{3.17}$$

where

$$\begin{aligned}
&I'_m = I'_m(kb), K'_m = K'_m(kb),\\
&p'_m = J_m(sa)Y'_m(sb) - Y_m(sa)J'_m(sb),\\
&r'_m = J'_m(sa)Y'_m(sb) - Y'_m(sa)J'_m(sb)
\end{aligned} \tag{3.18}$$

At the boundary $r = b$, we therefore have four equations:

$$\begin{aligned}
&\tilde{E}^d_{zm} = \tilde{E}^v_{zm}, \tilde{E}^d_{\theta m} = \tilde{E}^v_{z\theta m},\\
&\epsilon\tilde{E}^d_{rm} = \tilde{E}^v_{rm}, \tilde{B}^d_{zm} = \mu\tilde{B}^v_{zm}
\end{aligned} \tag{3.19}$$

which can be solve to yield the parameters ε_m, B_m, A_m, C_m.

For the monopole case $m = 0$, the longitudinal electric field for the region of interest $r_0 \leq r \leq b$ is given by

$$\tilde{E}_{z0} = \varepsilon_0' I_0(kr) + \eta_0' K_0(kr) \tag{3.20}$$

where

$$\varepsilon_0' = -\eta_0' \frac{(\mu\epsilon\beta^2 - 1)kK_0' + \gamma^{-2}\epsilon s p_0' K_0/p_0}{(\mu\epsilon\beta^2 - 1)kI_0' + \gamma^{-2}\epsilon s p_0' I_0/p_0} \tag{3.21}$$

In the limits $\gamma \gg \omega b/c$ and $kr \ll 1$, $\tilde{E}_{z0}$ in the latter equation reduces to

$$\tilde{E}_{z0} = \eta I_0(kr_0)\left(\frac{(\mu\epsilon - 1)p_0}{p_0' + (sb/2\epsilon)p_0}\frac{I_0(kr)}{\epsilon sb} - \frac{K_0(kr)}{\gamma^2}\right) \tag{3.22}$$

Using Eq. 3.4 and Eq. 3.22, we can get the monopole-case longitudinal electric field when $\gamma \to \infty$:

$$E_{z0}(r, z, t) = -\frac{ie\sqrt{\mu\epsilon - 1}}{\pi\epsilon bc} \times \int_{-\infty}^{\infty} d\omega e^{i\omega(z-ct)/c} \frac{p_0}{p_0' + (sb/2\epsilon)p_0} \tag{3.23}$$

Here $s = \omega\sqrt{\mu\epsilon - 1}/c$.

Then integrating Eq. 3.23 by the variable $x = sa$, for $z < ct$, we obtain

$$E_{z0}(r, z, t) = -\frac{4q}{\epsilon ab} \sum_{\lambda} \frac{x p_0}{(d/dx)D_0(x)} \times \cos\frac{x(z - ct)}{a\sqrt{\mu\epsilon - 1}}|_{x=x_\lambda} \tag{3.24}$$

where x_λ is the λth positive zero of the analytic function:

$$D_0 = xp_0' + \frac{x^2\xi}{2\epsilon}p_0 \tag{3.25}$$

Here $\xi = b/a$ is the ratio of the inner radius to the outer radius of the dielectric tube. Thus, we get the longitudinal electric field for the case of monopole(m=0).

For higher multipole fields, we can also get [18] the electric field for $z < ct$:

$$E_{zm}(r,z,t) = \frac{8q}{a^2}(\frac{r_0}{b})^m(\frac{r}{b})^m \times \sum_\lambda \frac{xp_m r_m}{(d/dx)D_m(x)} \cos\frac{x(z-ct)}{a\sqrt{\mu\epsilon-1}}|_{x=x_\lambda} \tag{3.26}$$

where

$$D_m(x) = (\frac{x^2\xi^2}{m+1} - m(\mu\epsilon+1))p_m r_m + x\xi(\epsilon p_m' r_m + \mu r_m' p_m) \tag{3.27}$$

Thus, for $m \neq 0$, E_{zm} does not vanish when $\gamma \to \infty$.

3.1.3 Transverse Force Due to Wakefield

Using the Eq. 2.12 from Panofsky-Wenzel theorem, we can get the transverse forces on the test charge e traveling with velocity v behind the source :

$$\tilde{F}_{rm} = \frac{ev}{i\omega}\frac{\partial\tilde{E}_{zm}}{\partial r} \tag{3.28}$$

$$\tilde{F}_{\theta m} = \frac{emv}{i\omega r}\tilde{E}_{zm} \tag{3.29}$$

Then using the Eq. 3.24, we can get the longitudinal force on the test particle of charge e at a distance z behind the leading source particle:

$$F_{z0}(z) = -\frac{eq}{a^2}\sum_{\lambda}\hat{F}_{z0\lambda}(x_{0\lambda})\cos\frac{x_{0\lambda}z}{a\sqrt{\epsilon-1}} \tag{3.30}$$

where

$$\tilde{F}_{z0\lambda} = \frac{4}{\epsilon\xi}\frac{x_{0\lambda}p_0(x_{0\lambda})}{D_0'(x_{0\lambda})} \tag{3.31}$$

Also, the transverse forces for $m \geq 1$ can be written as

$$F_{rm}(r,z;r_0) = \frac{eq}{a^2}(\frac{r_0}{a})^m(\frac{r}{a})^{m-1}\times\sum_{\lambda}\hat{F}_{rm\lambda}(x_{m\lambda})\sin\frac{x_{m\lambda}z}{a\sqrt{\epsilon-1}} \tag{3.32}$$

Here

$$\tilde{F}_{rm\lambda} = \frac{8m\sqrt{\epsilon-1}}{\xi^{2m}}\frac{p_m(x_{m\lambda})r_m(x_{m\lambda})}{D_m'(x_{m\lambda})} \tag{3.33}$$

The $x_{m\lambda}$ is the λth zero of D_m and the function D_m is already given by Eq. 3.27.

3.2 Implementation in PYTHON

The general wake potential for a relativistic beam passing through a dielectric-lined waveguide is simply the convolution between the density distribution and the wake function. The general wake function for a single mode structure is given by

$$w(z) = A\cos(kz) \tag{3.34}$$

where k and A are respectively the wave number and field amplitude associated with the fundamental mode (TM_{01}) of the structure. For these initial calculations, we assume a Gaussian distribution

$$\Lambda(z) = \frac{1}{\sqrt{2\pi}\sigma_z} e^{-\frac{z^2}{2\sigma_z^2}} \tag{3.35}$$

Then the wakefield can be written as the convolution of the wake function and the beam distribution as

$$W(z) = -\int_0^\infty \Lambda(z - z')w(z')dz' \tag{3.36}$$

The main challenge resides in the calculation of the wake function. To do so, one first needs to numerically solve the Eq. 3.24:

$$E_{z0}(r, z, t) = -\frac{4q}{\epsilon ab} \sum_\lambda \frac{xp_0}{(d/dx)D_0(x)} \times \cos \frac{x(z - ct)}{a\sqrt{\mu\epsilon - 1}}|_{x=x_\lambda}$$

by solving the dispersion equation Eq. 3.25:

$$D_0(x) = xp_0' + \frac{x^2\xi}{2\epsilon} p_0 = 0$$

Here $\xi = b/a$ is the ratio of the inner radius to the outer radius of the dielectric tube.

The algorithm used to solve the dispersion equation is described in the pseudo-code 1. In brief we seek x such as $D_0(x) = 0$ by varying the variable x by increment with step Δx until the sign between the values $D_0(x_i)$ and $D_0(x_i + \Delta x)$ changes. Knowing that $D_0(x)$ has a zero in $x \in [x_i, x_i + \Delta x]$, we implement a dichotomic method to find the root. The roots are labeled as x_m where m is an integer.

Algorithm 1 Solving Dispersion Equation

1: Choose x_i and adjust the step Δx ▷ Vary the x from x_i with an increasing step of Δx
2: Until $D(x_i)$ and $D(x_i + \Delta x)$ sign differs ▷ Determine the root between x_i and $x_i + \Delta x$
3: Use dichotomic method to find the root ▷ Solve the equation D(x)=0
4: Label this root as x_m ▷ the m-th root we find
5: Increase x with Δx as before ▷ until we find another root
6: Until we find N roots ▷ use a loop

The process is illustrated in Fig. 3.2 where we show the function $D_0(x)$ and the roots found by our algorithm. The red circles indicate the roots computed with our algorithm. The algorithm was tested over a wide range of parameters and found to be reliable provided that the step Δx is properly adjusted.

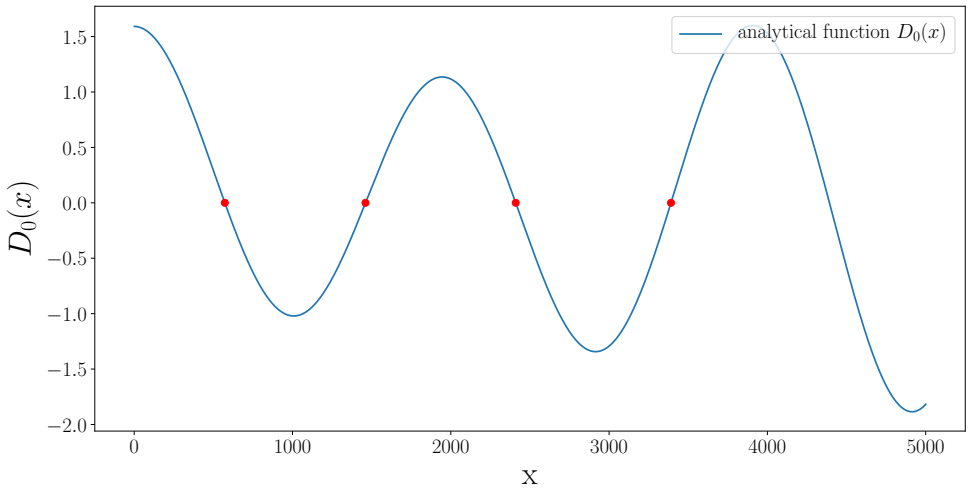

Figure 3.2: Dispersion equation $D_0(x)$ (blue trace).

Once the roots are obtained we can compute the electric field using Eq. 3.24 for the case of the monopole ($m = 0$) modes. Table 3.1 summarizes the roots and associated field amplitude computed for a DLW with parameters (a, b, ϵ_r) =(5 mm,2 mm,3).

Table 3.1: Summary of roots, wave vector and field amplitudes

n	1	2	3	4
roots x_λ	572.39	1460.93	2410.05	3390.97
mode amplitudes (V)	$1.47 \times 10^{+15}$	$1.85 \times 10^{+15}$	$1.28 \times 10^{+15}$	$7.27 \times 10^{+14}$
mode wave vectors (m^{-1})	404.74	1033.04	1704.16	2397.78

The corresponding wakefield computed by summing a different number of modes appear in Fig. 3.3.

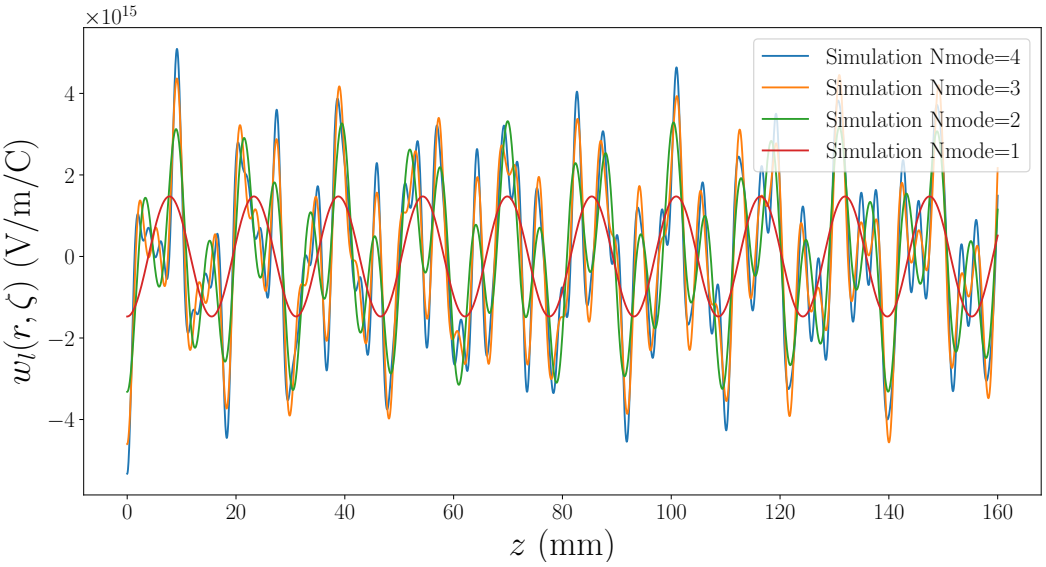

Figure 3.3: Longitudinal wake function computed by the PYTHON for different Nmodes.

In most of our computations we generally find that the wakefield function is well described by a summation over the first four modes; the contribution from higher modes becomes negligible as illustrated in Fig. 3.3.

The comparison of the wakefield computed for $N_{modes} = 4$ and 10 appears in Fig. 3.4.

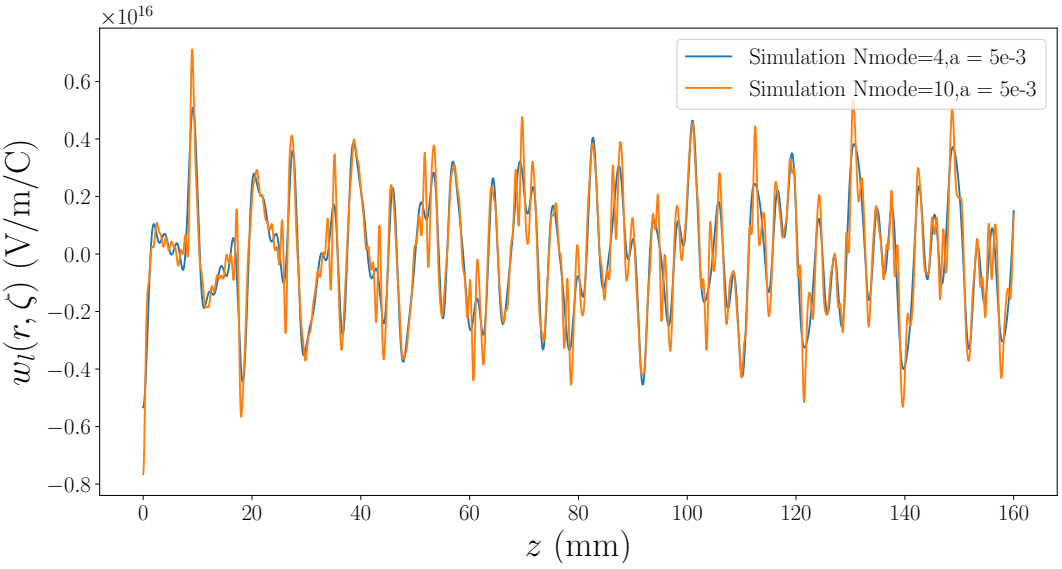

Figure 3.4: Wakefield $w_l(z)$ computed by the PYTHON program with different m.

As it can be seen from the Fig. 3.4, the case $N_{modes} = 4$ provides an accurate description of the wakefield. Summing higher order modes introduces higher frequency features but does not significantly affect the overall amplitude of the wakefield. Likewise, because of the convolution integral Eq. 2.9, the high-frequency features tend to generally get smoother on the wake potential.

In order to gain confidence in our algorithm, we benchmarked it with a trusted commercial code developed by Euclid TechLab; see Fig. 3.5. We specifically consider the case of a DLW with parameter (a, b, ϵ_r) =(5 mm , 2 mm, 3) and a bunch charge of 100 nC. The results from our program are found to be in excellent agreement with this commercial software.

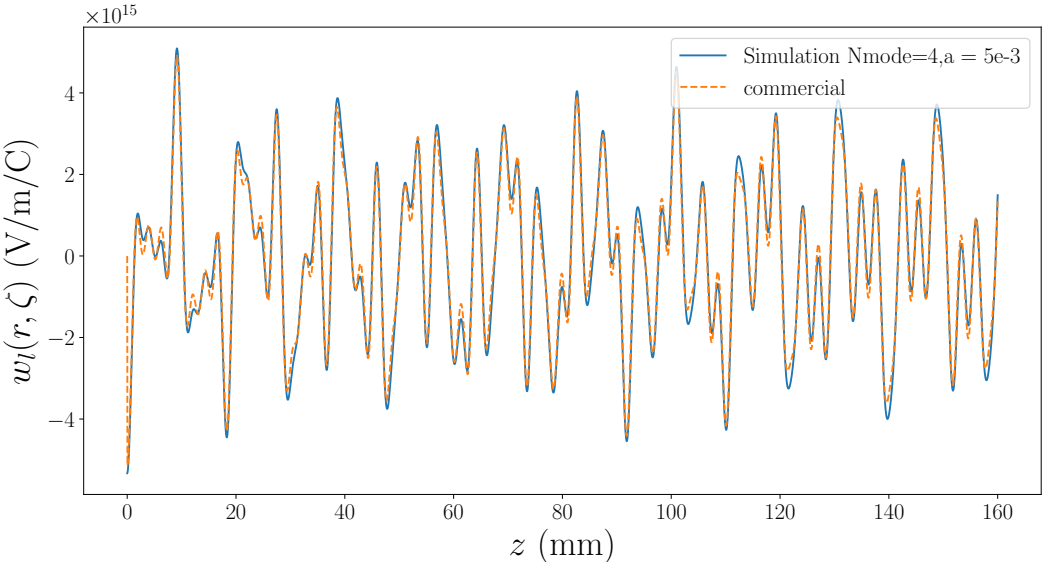

Figure 3.5: Wakefield $w_l(z)$ computed by the PYTHON program (blue trace) and a commercial program (orange trace).

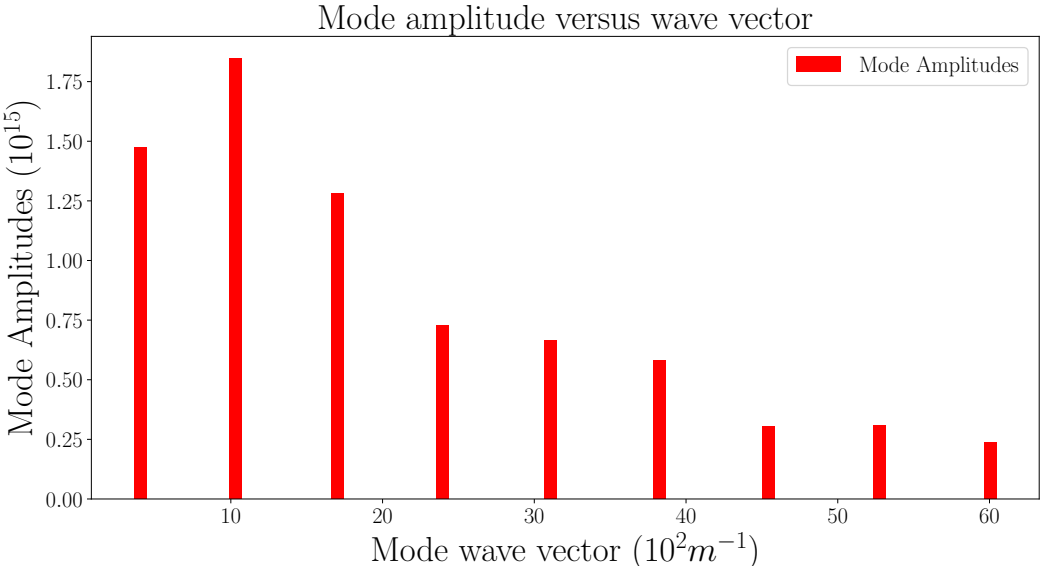

Figure 3.6: Wave modes amplitude vs wave vector.

Also, we need to note here that we make the electron bunch travel through the dielectric lined tube with an offset relative to the center of the axis, so the offset $r_0 = b/2$.

Also, we can get the relation between the wave mode and wave length as in Fig. 3.6. As we can see, the mode amplitude eventually decays to small values.

An algorithm similar to the one described above was used to find the multipole-mode ($m > 1$) wakefield. The dispersion equation Eq. 3.27:

$$D_m(x) = (\frac{x^2\xi^2}{m+1} - m(\mu\epsilon + 1))p_m r_m + x\xi(\epsilon p'_m r_m + \mu r'_m p_m)$$

can be solved. An example of root findings is shown in Fig. 3.7 where the dipole mode ($m = 1$) is considered.

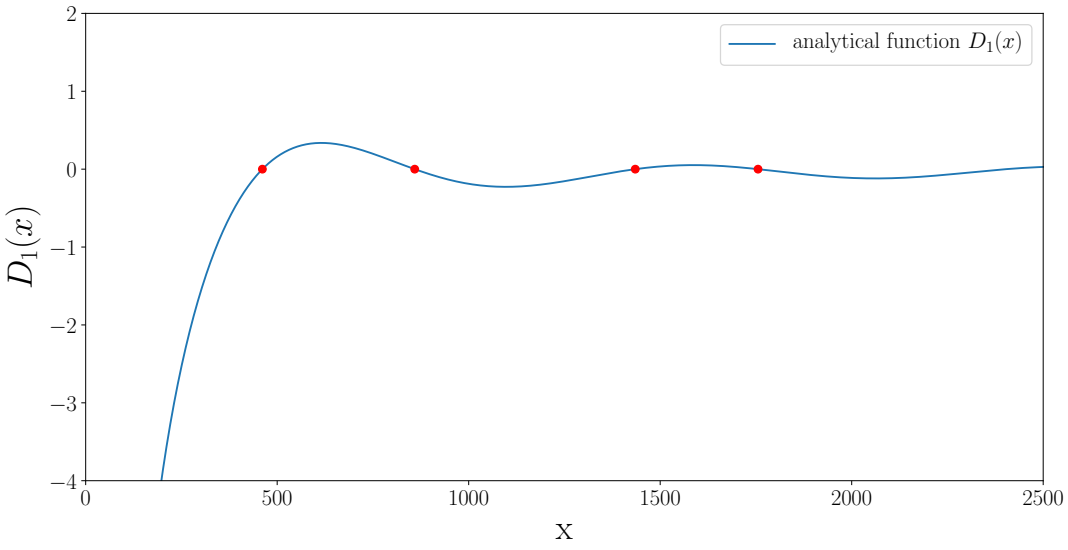

Figure 3.7: Dispersion equation plot when m=1. The red points are the roots.

The first four roots x_λ are [461.36, 859.11, 1434.90, 1755.46]. Table 3.2 summarizes the roots and associated field amplitudes and wave vectors for the dipole mode ($m = 1$)

computed for a DLW with parameters (a, b, ϵ_r) =(5 mm , 2 mm,3.0) identical to the ones used in Table. 3.1.

Table 3.2: Summary of roots, wave vector and field amplitudes

n	1	2	3	4
roots x_λ	461.36	859.11	1434.90	1755.46
mode amplitudes (V)	$3.43 \times 10^{+17}$	$2.42 \times 10^{+18}$	$2.53 \times 10^{+18}$	$3.68 \times 10^{+18}$
mode wave vectors (m^{-1})	326.23	607.48	1014.63	1241.30

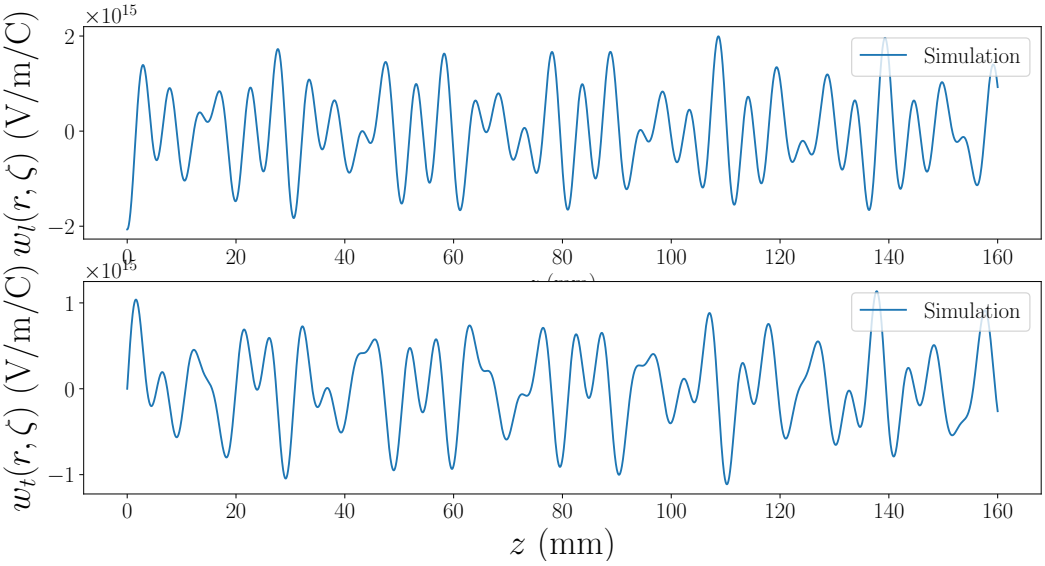

Figure 3.8: Longitudinal (top) and transverse (bottom) wake functions for $m = 1$.

The corresponding longitudinal wakefield is shown in Fig 3.8 (upper plot). For $m \geq 1$ the fields do also have transverse components and an example of transverse wakefield appears in Fig 3.8 (lower plot). For the results presented in Fig 3.8, the number of modes was taken to be $N_{modes} = 4$. Also, in order to gain confidence in our algorithm for the transverse wakefield, we benchmarked it with a trusted commercial code developed by Euclid TechLab; see Fig. 3.9. The DLW parameters are identical to those used in Table. 3.1.

Finally, using Eq. 3.36 we can compute the wakepotential of a Gaussian distribution beam. The result is shown in Fig. 3.10 and Fig. 3.11 for respectively the longitudinal electric

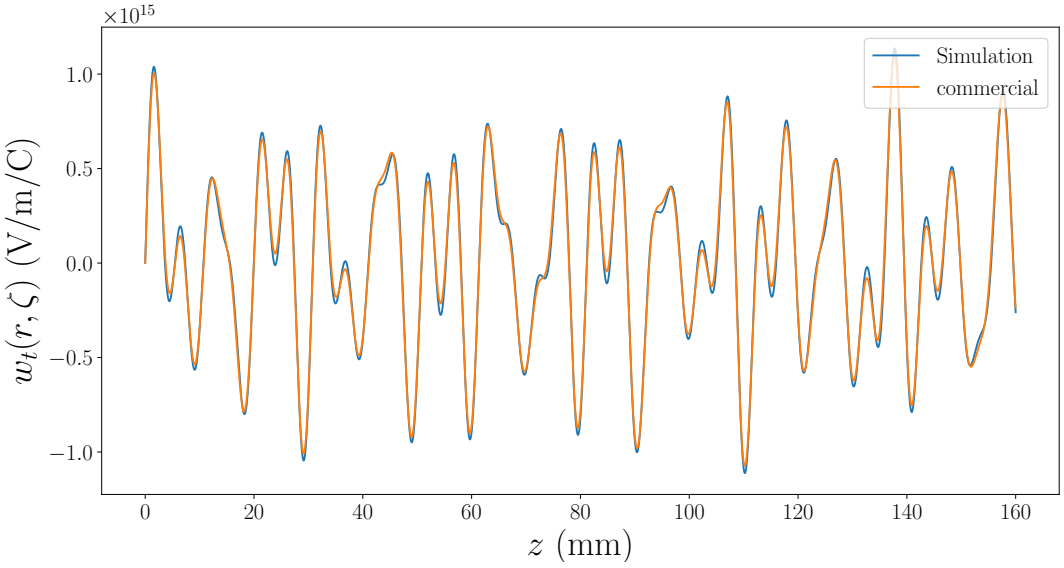

Figure 3.9: Transverse wake function compared with a commercial code.

field and transverse force. The length of the electron bunch traveling path is $160\sigma_z$, and the bunch length was taken to $\sigma_z = 1.0 \times 10^{-3}$ m with charge of 100 nC.

As we can see in Fig. 3.10, the considered Gaussian bunch can generate wakefield on the order of 0.1 GV/m trailing behind the bunch. In this example an electron located at $z/\sigma_z \simeq 27$ would experience the field and get accelerated. This process is often referred to beam-driven wakefield acceleration. This acceleration mechanism is being investigated at several facilities, including the Argonne Wakefield Accelerator [27]. Unfortunately, the transverse force can be quite high and particles within the Gaussian bunch can be deflected if the beam is not properly aligned. This effect is an important limitation of wakefield accelerators.

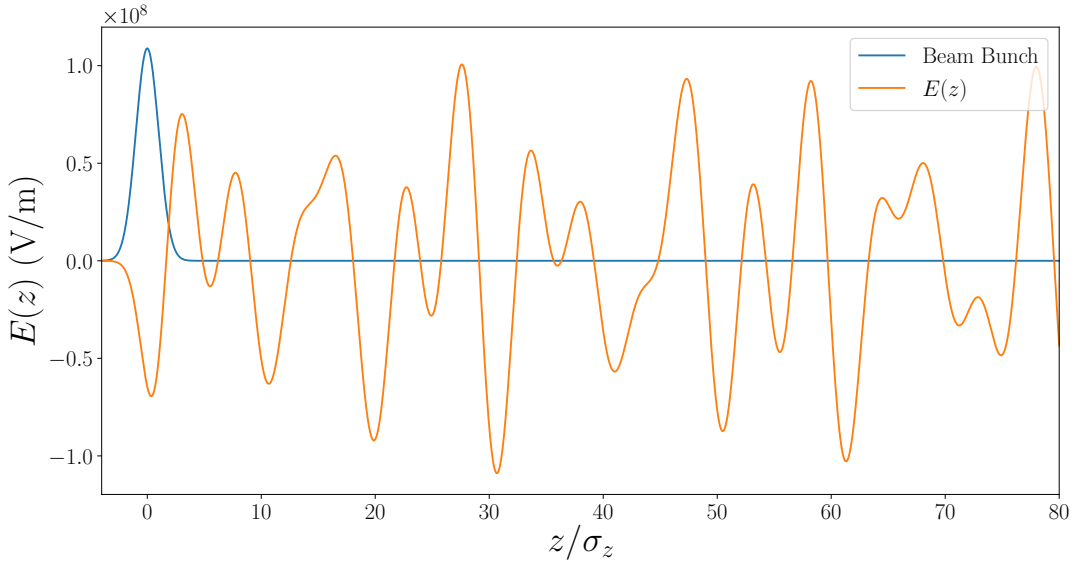

Figure 3.10: Longitudinal electric field (orange trace) generated by a Gaussian charge distribution (blue trace). The charge distribution moves toward $z < 0$.

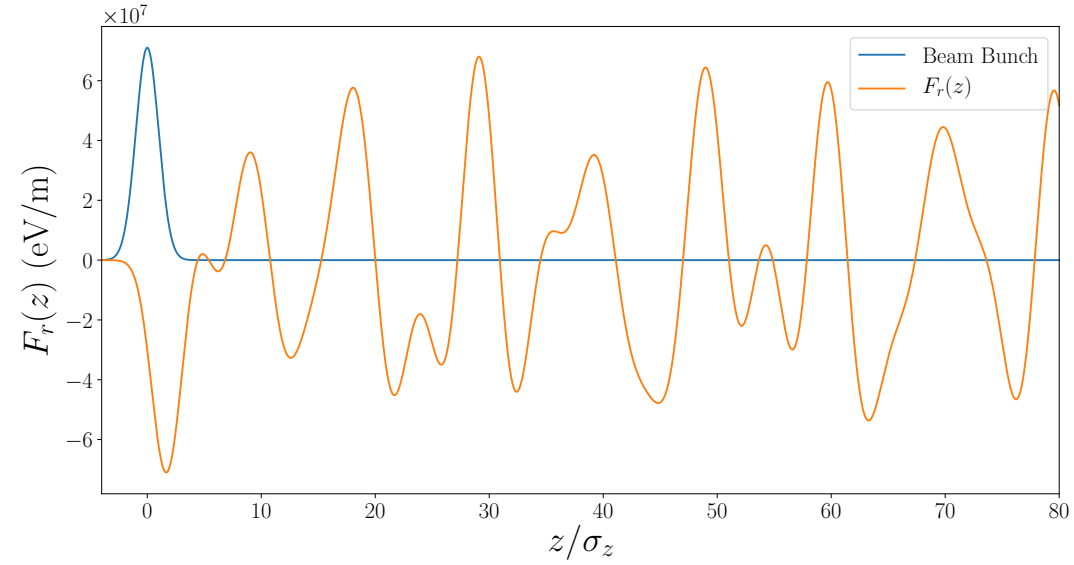

Figure 3.11: Transverse force (orange trace) generated by a Gaussian charge distribution (blue trace). The charge distribution moves toward $z < 0$.

CHAPTER 4

WAKEFIELD AS A DIAGNOSTIC

In this chapter we explore a method to use the transverse wakefield to passively streak the beam and infer its temporal (or longitudinal) distribution. Before delving in the wakefield technique, we recall the working principle of streaking by considering an RF transverse deflecting cavity.

4.1 Beam Dynamics in the Presence of Time-dependent Transverse Deflecting Field

We consider a beam which consists of N electrons with the distribution function $\rho(z)$; z is the distance from the particle along the traveling path. Using the SI unit, the change in the longitudinal momentum of the particles at location z is given by the integral

$$\Delta p_z(z) = Ne^2 \int_z^\infty dz' \rho(z') w_l(z' - z) \tag{4.1}$$

In order to quantify the beam dynamics, it is often convenient to introduce $\zeta(t) \equiv z(t) - c\int_0^t \beta(t')dt'$, where ζ represents the axial position of an electron with respect to the bunch center ($\zeta = 0$) at the time t. Since the beam dynamics also involves the momenta, we introduce p_i the conjugate momenta associated to the spatial coordinates $i = x, y, \zeta$ and note that for a bunch $p_\zeta \gg (p_x, p_y)$. For convenience we also introduce the angular divergence as

$x' \equiv \frac{p_x}{p_z}$ and $y' \equiv \frac{p_y}{p_z}$. Finally we introduce the relative momentum spread as $\delta \equiv \frac{p}{\langle p \rangle}$ where $p^2 = p_x^2 + p_y^2 + p_z^2$.

In order to describe the dynamics of a bunch in presence of transverse wakefield, it is often useful to describe the bunch as an ensemble of axial slices. The transverse position of these slices at a given position z along the beamline is a function of ζ and parameterized as $\boldsymbol{x}(\zeta, z)$, where the vector $\boldsymbol{x} \equiv (x, y)$. Considering the case of a transverse wakefield giving rise to the transverse Green's function $w_\perp(\zeta)$ along, e.g., the x direction, we can write the corresponding transverse horizontal force as

$$F_x(\zeta, z) = e^2 \int_\zeta^\infty d\zeta' \rho(\zeta') w_\perp(\zeta - \zeta') x(\zeta', z) \tag{4.2}$$

where e is the electronic charge. Consequently the transverse equation of motion can be written as [28, 29]

$$\begin{aligned} \frac{d}{dz}\left[\gamma(z)\frac{d}{dz}x(\zeta, z)\right] + K^2\gamma(z)x(\zeta, z) = \\ r_0 \int_\zeta^\infty d\zeta' \rho(\zeta') w_\perp(\zeta - \zeta') x(\zeta', z), \end{aligned} \tag{4.3}$$

where $r_0 \equiv \frac{e}{mc^2}$ is the classical radius of the electron, $\gamma \equiv \frac{\mathcal{E}}{mc^2}$ is the relativistic Lorentz factor (here $\mathcal{E}^2 \equiv p^2c^2 + m^2c^4$ is the total energy), and K describes external focusing fields.

In a drift space ($K = 0$) and assuming the beam energy remains unchanged, $\gamma(s) = \gamma$ and $\frac{d\gamma}{dz} = 0$, the latter equation simplifies to

$$\frac{d^2x(\zeta, z)}{dz^2} = \frac{r_0}{\gamma} \int_\zeta^\infty d\zeta' \rho(\zeta') w_\perp(\zeta - \zeta') x(\zeta', z) \tag{4.4}$$

Taking the wakefield to be constantly applied over a length L, the previous equation can be integrated to yield

$$\begin{aligned} x'(\zeta, z) &= \frac{dx(\zeta, z)}{dz} \\ &= \frac{Lr_0}{\gamma} \int_{\zeta}^{\infty} d\zeta' \rho(\zeta') w_{\perp}(\zeta - \zeta') x(\zeta', z) \end{aligned} \tag{4.5}$$

The most-left equality is valid under the ultra-relativistic approximation $\gamma \gg 1$. Assuming that the slice position does not change during the interaction but only its divergence is affected (this is the so-called "impulse approximation"), we can further simplify the previous equation into

$$\begin{aligned} x'(\zeta, z) &= \frac{dx(\zeta, z)}{dz} \\ &= x(\zeta, z) \frac{Lr_0}{\gamma} \int_{\zeta}^{\infty} d\zeta' \rho(\zeta') w_{\perp}(\zeta - \zeta') \end{aligned} \tag{4.6}$$

This equation is the basis of transverse wakefield calculation: Knowing the longitudinal charge distribution $\rho(\zeta)$ and the transverse Green's function describing the electromagnetic wake, one can infer the transverse displacement of longitudinal slices.

4.2 Streaking Field as Bunch Length Diagnostics

We now consider the possible use of transverse wake to streak the beam aka to what is commonly done with a transverse deflecting cavity. This possibility was explored in Ref. [17] where it was pointed out that one could in principle reconstruct the longitudinal distribution and some preliminary results were presented.

4.2.1 Analysis of the Active Transverse Deflector

A common time-domain diagnostic method to infer the duration of sub-picoseconds employs a transverse-deflecting resonant radiofrequency (RF) cavity [29]. The cavity usually operates on the TM_{110} mode and therefore sustains a transverse time-dependent magnetic field B. As the bunch travels through the cavity [30], it results in a transverse kick (e.g. in the x direction) of the form

$$x'(\zeta, z) \simeq \frac{Lr_0E_0}{\gamma} \sin(k\zeta + \varphi) \tag{4.7}$$

where L is now the length of the cavity, E_0 the peak electric field provided by the cavity and φ is an arbitrary phase shift we henceforth take to be $\varphi = 0$, and $k = \frac{2\pi}{\lambda_{rf}}$ is the wave vector associated to the wave supported by the RF cavity. In practice, the bunch length σ_ζ is such that $\sigma_\zeta \ll \lambda_{rf}$ so that the sin() function can be approximated by its first-order Taylor expansion. In such a case we have

$$x'(\zeta, z) = \frac{Lr_0E_0}{\gamma} k\zeta \equiv \kappa\zeta \tag{4.8}$$

and the kick is linearly dependent on the bunch longitudinal coordinate. In the previous equation κ is referred to as the normalized kicking strength. A typical experimental setup for measuring the longitudinal bunch distribution consists in recoding the transverse distribution $f_x(x)$ downstream of the deflecting cavity. To analyze such a measurement we recall that the transverse phase-space coordinate $\boldsymbol{x} \equiv (x, x')$ downstream of a beamline with transfer matrix R is given by $\boldsymbol{x} = R\boldsymbol{x}_0$, where x_0 is the initial coordinate upstream of the beamline.

Taking R to be the transfer matrix from the cavity exit to the observation point, we can write for the position of one electron:

$$x = R_{11}x_0 + R_{12}x'_0 \tag{4.9}$$

where $x'_0 = \kappa\zeta + x'_{0,-}$ with $x'_{0,-}$ understood as the electron's initial angle prior to receiving the deflecting kick. Under such an assumption the horizontal position of an electron at the observation point reduces to

$$\begin{aligned} x &= R_{11}x_0 + R_{12}(\kappa\zeta + x'_{0,-}) \\ &= R_{11}x_0 + R_{12}x'_{0,-} + R_{12}\kappa\zeta \equiv x_\beta + R_{12}\kappa\zeta \end{aligned} \tag{4.10}$$

where x_β is the change of position due to the betatronic motion. The latter equation can be rewritten as

$$x = x_\beta + x_\zeta \tag{4.11}$$

which simplifies to $x = x_\zeta$ when the deflector is turned off. Introducing the probability distribution for x_β and x_ζ to be respectively $f_\beta(x_\beta)$ and $f_\zeta(x_\zeta)$ and further considering the variables to be independent, the probability distribution associated to x is given by the convolution

$$f(x) = \int_{-\infty}^{+\infty} f_\beta(x_\beta) f_\zeta(x - x_\beta) dx_\beta \tag{4.12}$$

The longitudinal distribution is related to $f_\zeta(x)$ via the charge conservation relation $f_\zeta(x)dx = \rho(\zeta)d\zeta$ that is $\rho(\zeta) = |R_{12}\kappa| f_\zeta(R_{12}\kappa\zeta)$. Therefore we need to extract the function $f_\zeta(x)$ from Eq. (4.12). We note that $f(x)$ and f_β can be directly measured by recording the distribution

at the observation point respectively with and without powering the deflecting cavity. One can then perform a deconvolution [31] to retrieve $f(x)$. Another possibility is to ensure the beta function at the observation point is very small so that $f_\beta(x_\beta) \simeq \delta(x_\beta)$, where $\delta()$ is the Dirac's function. Consequently Eq. (4.12) can be simplified to $f(x) \simeq f_\zeta(x)$.

4.2.2 Equations for a Passive Deflector

Given the description of the active deflection scheme, we can now modify the previous equations to apply them to the passive deflection technique. Equation (4.10) is especially modified as

$$x = x_\beta + R_{12} x'_0(\zeta) \tag{4.13}$$

where $x'_0(\zeta) \equiv x'(\zeta, z = 0)$ with $z = 0$ corresponding to the position where the kick is applied (i.e. the center of the deflecting structure in the impulse approximation); see Eq. (4.6). We point out that $x_\zeta \equiv R_{12} x'_0(\zeta)$ is now a nonlinear function of ζ.

4.3 Algorithm to Reconstruct the Longitudinal Beam Profile

Using the equation for a passive deflector $x_\zeta \equiv R_{12} x'_0(\zeta)$ in the previous chapter, the charge conservation relation $f_\zeta(x)dx = \rho(\zeta)d\zeta$ can be written as

$$\rho(\zeta) = |R_{12} \frac{dx'_0(\zeta)}{d\zeta}| f_\zeta(x) \tag{4.14}$$

Here we can get the derivative $\frac{dx_0'(\zeta)}{d\zeta}$ from Eq. 4.6. The wake function then can be obtained from Eq. 4.6; here the transverse wake function is the numerical result along ζ when the beam travels through the waveguide with offside $r_0 = b/2$.

Thus, through substituting the already known wake function in Eq. (4.6), we can obtain the derivative $\frac{dx_0'(\zeta)}{d\zeta}$. After we extract $f_\zeta(x)$ from Eq. (4.12), the rest of the problem is to solve the self-consistent equation for the probability distribution $\rho(\zeta)$ along ζ. Since we can measure the probability distribution on the monitor, we can directly obtain the values of $f(x)$ and the probability distribution $f_\beta(x)$ when the deflecting is turned off in Eq. (4.12). Then we can use the deconvolution method to extract the longitudinal distribution $f_\zeta(x)$. Finally, we can get the longitudinal distribution $\rho(\zeta)$ through Eq. (4.14).

The algorithm implemented to retrieve the longitudinal bunch distribution $\rho(\zeta)$ from the observed distribution $f_\zeta(x)$ consists of an iterative method summarized in the pseudo-code 2. The algorithm we selected is a simple adaptive loop commonly used in feedback control systems. Specifically, we first make a guess of the longitudinal charge density $\rho(\zeta)$ and compute the corresponding projected function $f_\zeta(x)$ from which the incoming charge density is recovered. The adaptive loop consists in readjusting the initial longitudinal charge density given as detailed in the pseudo-code 2.

The latter algorithm was implemented as a PYTHON script dubbed STREAK.PY. The program reads an external particle distribution and simulates the streaking effect due to the wakefield (by using use the Eq. 3.32) and transports the particle down to the observation point where the transverse distribution is measured. The script STREAK.PY finally gives the distribution and implements the iterative algorithm described in the pseudo-code 2 to retrieve the initial distribution. The retrieved and initial distributions can then be compared to verify the effectiveness of the reconstruction algorithm.

Algorithm 2 Longitudinal Charge Distribution Retrieval

define $\mathcal{G}$ ▷ gain for the adaptive loop
read $f_\zeta^m(x)$ ▷ measured beam profile after deconvolution
initialize $\rho_0(\zeta)$ ▷ initial (guessed) charge distribution
for $i \in [0, N]$ **do**
    $x(\zeta)$=TransWake[Green, $\rho_i(\zeta)$] ▷ compute deflecting kick for a given Green's function
    $f_\zeta(x)$=Streak[$\rho_i(\zeta)$, $x(\zeta)$] ▷ evaluate streaked profile
    $\rho_i^e(\zeta) = f_\zeta(x) \times |\frac{dx}{d\zeta}|$ ▷ estimated charge distribution from streaked profile
    $\rho_{i+1}(\zeta) = \rho_i + \mathcal{G} \times (\rho_i^e(\zeta) - \rho_i)$ ▷ successive approximation
    $\epsilon_i = \sum_x [|(f_\zeta(x) - f_\zeta^m(x))|]$
end for
plot $\rho_N(\zeta)$

4.4 Simulations

A step toward more accurate simulation is to use the beam-dynamics program ELEGANT [32] to perform the tracking and wakefield simulation up to the observation point. The obtained streak distribution is then passed to the STREAK.PY to reconstruct the initial distribution.

4.4.1 Cold-Beam Reconstruction

We first apply the reconstruction algorithm to the case of a cold beam, e.g., a beam where the distribution has no transverse extent and can be viewed as a line charge. The reason for testing the case of the cold beam is to focus solely on the longitudinal-to–transverse mapping provided by the DLW without dealing with smearing effect due to the finite transverse dimension associated with a real beam (that is, a beam with nonzero transverse emittance).

As a first illustration, we start with a Gaussian distribution shown in Fig. 4.1.

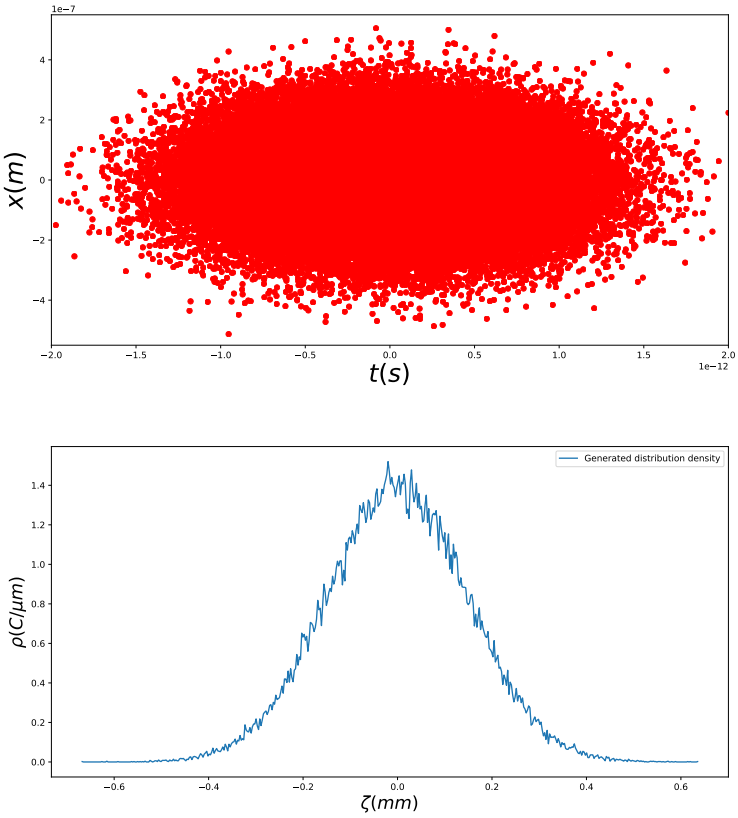

Figure 4.1: Gaussian distribution on the side of the axis t and x

Here the bunch has a total charge of 1×100 nC with a total number of macroparticle of $100,000$. For the rest of this chapter we take the DLW used to streak the beam to have the following parameters: an inner radius of $b = 4.50 \times 10^{-4}\,\mathrm{m}$, an outer radius of $a = 5.50 \times 10^{-4}\,\mathrm{m}$ and the dielectric constant of the medium is $\epsilon = 4.41$. We also consider the observation point where the transverse distribution is finally observed to consist of a 1-m drift space so to have $R_{12} = 1.0\,\mathrm{m}$; a diagram of the setup appears in Fig. 4.2.

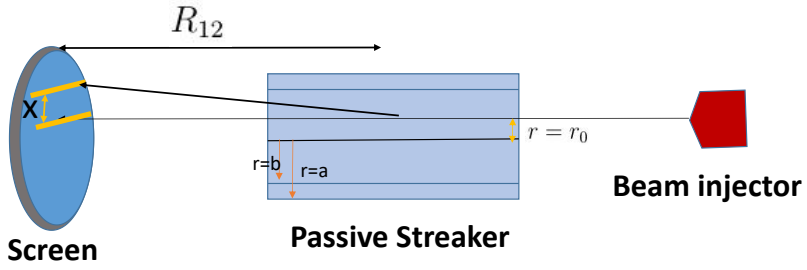

Figure 4.2: Configuration used for the simulation of the passive-streaking temporal diagnostics.

In the PYTHON code, we simulate the streak as the sum of the monopole and dipole transverse forces, and the effect would be as in Fig. 4.3.

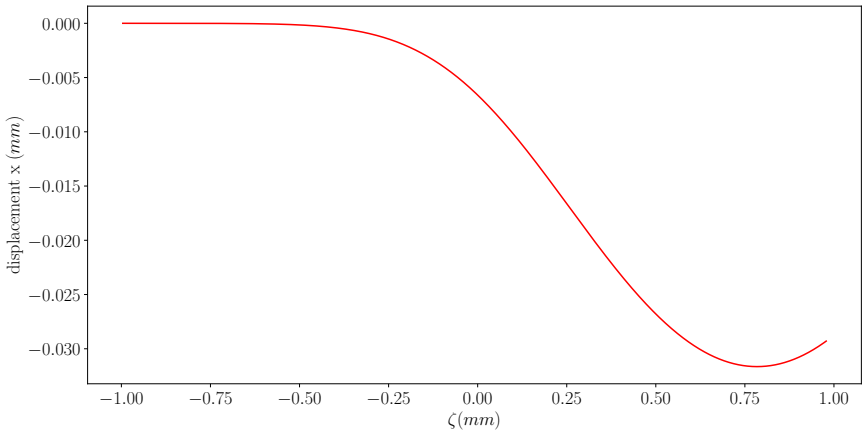

Figure 4.3: Wakefield as a transverse streak on the beam of zero emittance along the longitudinal path.

The beam bunch is originally a beamline along the axis of the tube; in Fig. 4.3, it is traveling along the t axis, here it is the path along the traveling direction. But as it travels with an offset of $r = b/2$, the self-generated wakefield then produces a streak on itself as shown in the Fig. 4.3.

As the Eq. 4.14 indicates, we have to get $f_\zeta(x)$ before we get the longitudinal density function of the beam bunch $\rho(\zeta)$. The question now is to find the density function $f_\zeta(x)$ on the screen along the transverse direction x. Fortunately, we can measure the density function $f_\zeta(x)$ of the beam bunch on the screen directly. In this simulation, the streaked beam density on the screen is shown in Fig 4.4. The horizontal axis here is the x on the screen and the

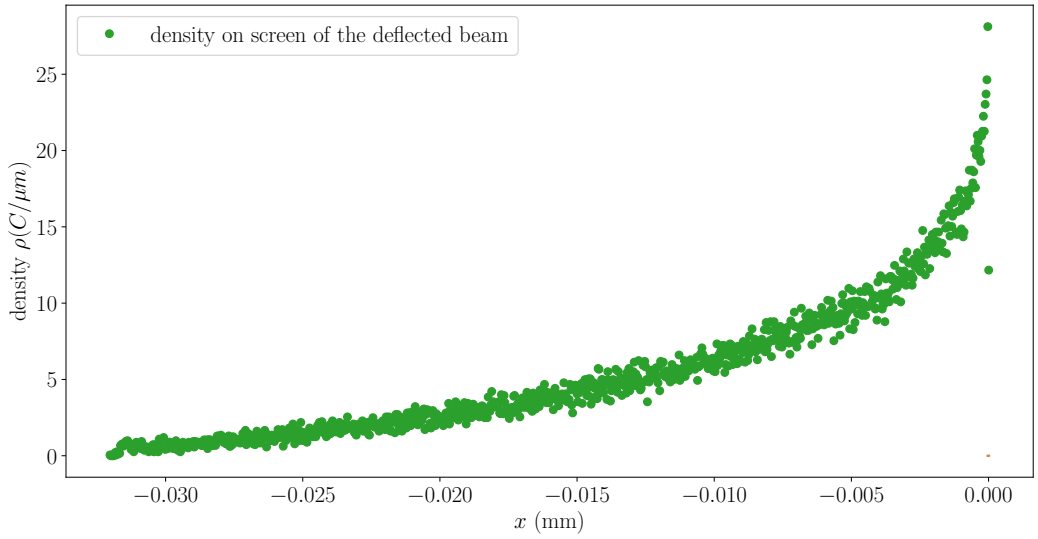

Figure 4.4: Density of the deflected beam of zero emittance along the transverse direction x

vertical axis is the density. After we get the $f_\zeta(x)$, then the iterative algorithm can be used. Finally, after just 20 iterations, the result is pretty good, as shown in Fig. 4.5.

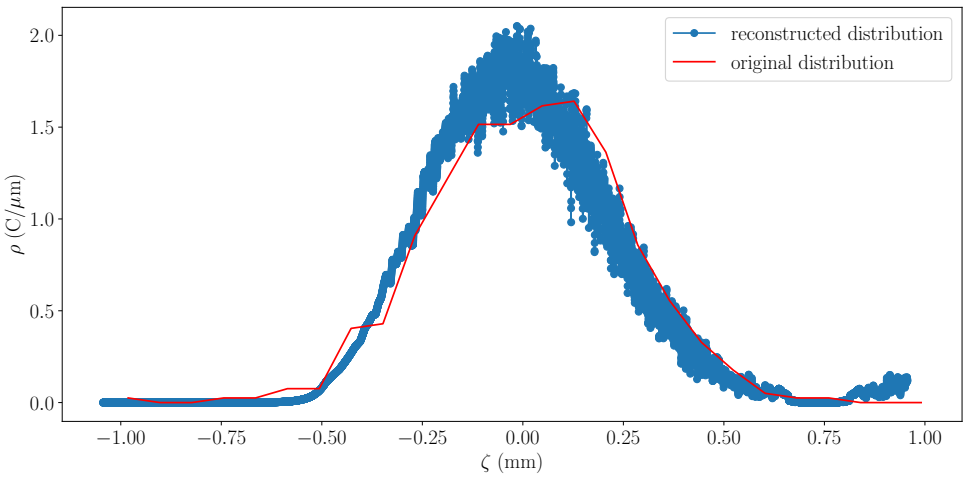

Figure 4.5: Comparison of the reconstructed density profile of the zero-emittance beam in the longitudinal direction.

Here the blue dots are the reconstructed density profile of the beam bunch, and the red line is the original generated beam bunch profile.

We now consider a more intricate distribution taken to be temporally modulated as a sum of Gaussian distributions. In this case, the initial guess is a single Gaussian curve and the iteration shows the conversion process ultimately retrieving the modulated distribution; see Fig. 4.6.

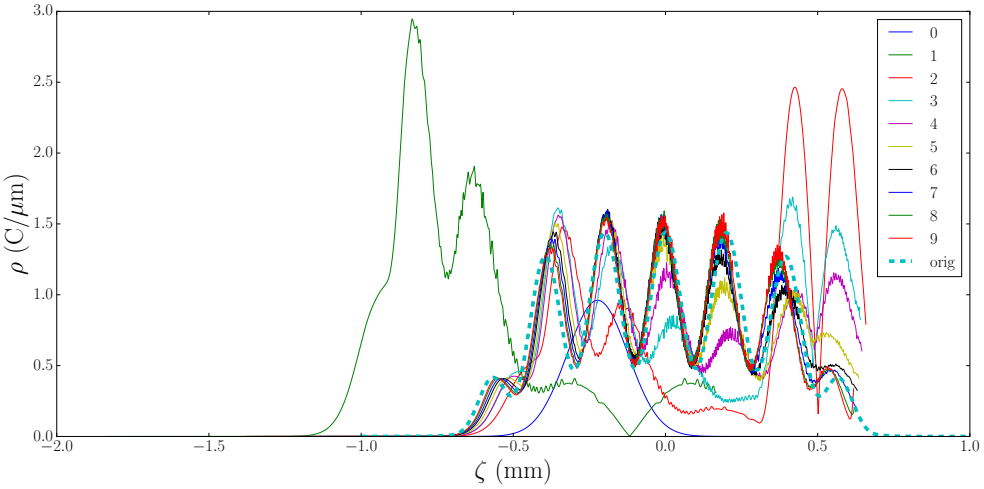

Figure 4.6: Evolution of the retrieved distribution functions for the 10 iteration steps.

A derailed comparison of the final retrieved distribution is shown in Fig. 4.7. The result of retrieved distribution after 20 iterations (blue symbol) compared to initial distribution (red trace) is in good agreement with the input distribution used.

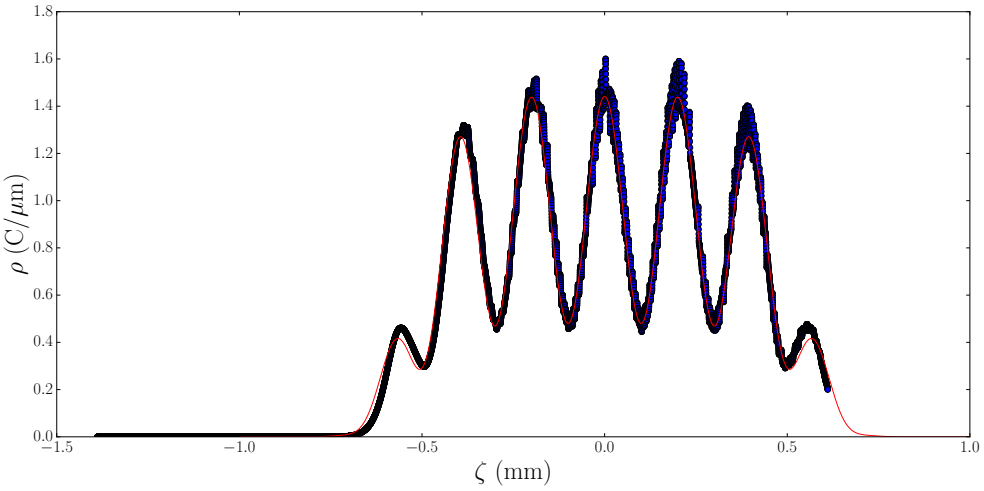

Figure 4.7: Retrieved distribution after 20 iterations compared to initial distribution.

4.4.2 Case of Nonzero-Emittance Beam Reconstruction

We now test our algorithm for the case of a non-vanishing transverse emittance. The transverse emittance is a measure of the spread of particle coordinates in position-and-momentum phase space and has the dimension of length (e.g. meters) or length times angle (meters times radians). A statistical definition of the emittance, which is the so-called normalized rms emittance, is defined as

$$\varepsilon_{n,rms} = \frac{1}{m_0 c}\sqrt{< x^2 >< p_x^2 > - < xp_x >^2} \tag{4.15}$$

where <> is defined as

$$< x^2 >= \frac{\sum x^2}{n} - (\frac{\sum x}{n})^2, < p_x^2 >= \frac{\sum p_x^2}{n} - (\frac{\sum p_x}{n})^2, \tag{4.16}$$

$$< xp_x >= \frac{\sum xp_x}{n} - (\frac{\sum x \sum p_x}{n^2}) \tag{4.17}$$

and all sums are performed for the n particles in the distribution, i.e., $\sum x = \sum_{i=1}^{n} x_i$. It is proportional to the area of the phase space ellipse without a constant factor π. The parameter of emittance describing a particle beam in phase space is a powerful tool in beam dynamics, and it can be proved that the density of particles in phase space does not change along a beam transport line, where the forces acting on particles can be derived from macroscopic electric and magnetic fields[33]. Thus, knowing the area occupied by particles in phase space at the beginning of a beam transport line will allow us to determine the location and distribution of the beam without having to calculate the trajectory of every individual particle. After the beam passes through the dielectric-lined tube, it is received on the downstream screen.

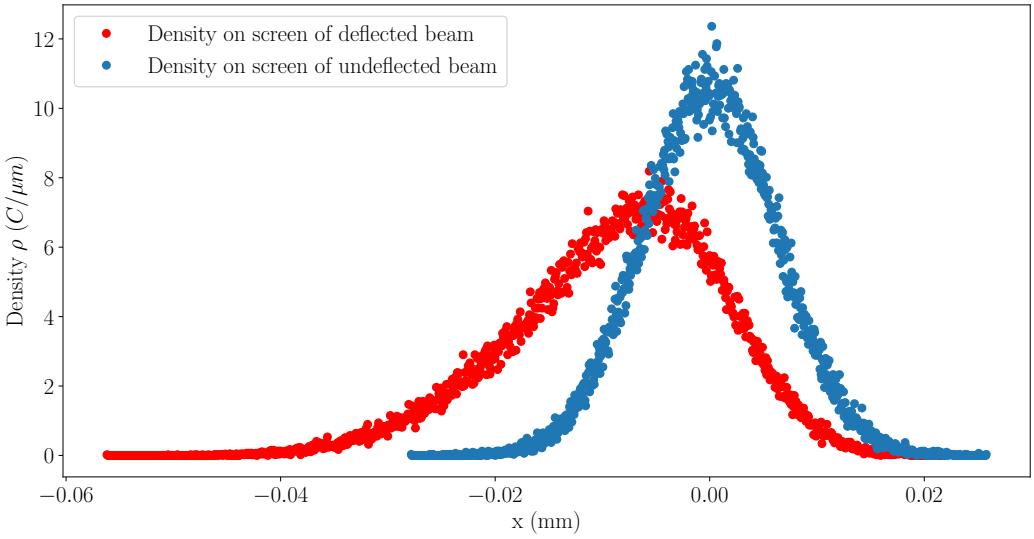

Figure 4.8: Density profile of the nonzero-emittance beam on screen.

We can see the density of the beam $f_\zeta(x)$ in Fig. 4.8. We can see the density profile of the nonzero-emittance beam on screen in the transverse direction traveling with off axis and on axis. The red points line is the density that is deflected by the wakefield because the beam bunch travels through the dielectric-lined tube with an offset of $r_0 = b/2$, which gives the beam a transverse deflecting effect. And the blue points are the density when the beam is received on the downstream screen. As we can see, this beam is not deflected because it travels through the tube without an offset relative to the center axis; thus, no transverse deflecting force is produced on the beam itself.

Next, we need to deconvolve the Eq. 4.12 to get the $f_\zeta(x)$ for the iterative algorithm. After 20 iterations, the retrieved beam distribution $\rho(\zeta)$ is shown in Fig. 4.9. Here the blue line is the reconstructed density profile of the beam bunch, and the red line is the original generated beam bunch profile.

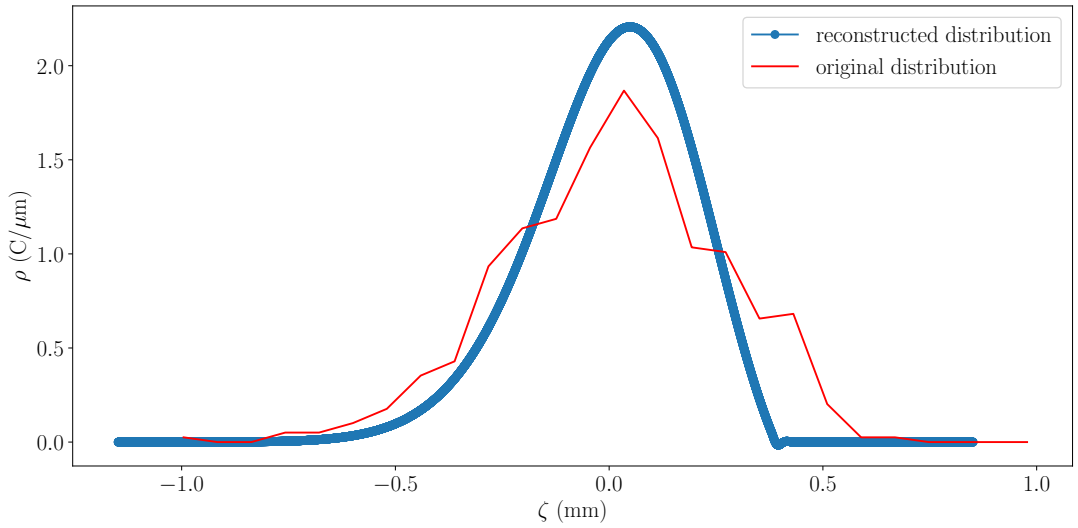

Figure 4.9: Comparison of the density profile of the reconstructed nonzero-emittance beam.

CHAPTER 5

CONCLUSION

The measurement of ultra-short electron bunch produced in high-energy accelerators is crucial to many applications. Yet such a measurement is intricate and to date the most reliable measurement relies on a transverse deflecting cavity which, given its high cost, is limited to few accelerator facilities.

The present thesis explored a passive technique based on the use of electromagnetic wakefield produced as an electron bunch propagated off axis in a dielectric-lined waveguide. The wakefields introduce a time-dependent transverse force which effectively streaks the bunch. Consequently, the simple measurement of the bunch transverse distribution provides information on the bunch current profile.

In this thesis we first contributed to the development of an open-source program capable of computing the electromagnetic field in a dielectric-lined waveguide. We introduced the Green's function computed by the program into the popular tracking program ELEGANT and simulated the proposed passive diagnostics.

We finally developed an iterative method to reconstruct the temporal profile of an electron bunch and investigated its performances. In summary, the explored technique is promising and the exploratory work performed under this thesis will serve as a basis for a possible experimental investigation at the FAST/IOTA facility at Fermilab.

REFERENCES

[1] The free electron laser was first proposed by John Madey in 1971; see J.M.J. Madey, J. Appl. Phys., **42**, 1906 (1971). Madey's concept was actually predated by similar concepts for the amplification of microwave radiation; R.M. Philips, IRE Trans. Electron Devices, 7, 231 (1960).

[2] D. A. G. Deacon, L. R. Elias, J. M. J. Madey, G. J. Ramian, H. A. Schwettman, and T. I. Smith, Phys. Rev. Lett. 38, 892 (1977).

[3] Luis R. Elias, William M. Fairbank, John M. J. Madey, H. Alan Schwettman, and Todd I. Smith, Phys. Rev. Lett. 36, 717 (1976).

[4] C. Pellegrini, Physica Scripta, Volume 2016, paper Number T169 (2017).

[5] Peter Baum and Ahmed H. Zewail, *Proceedings of the National Academy of Sciences* Oct 2006, 103 (44) 16105-16110 (2006).

[6] See for instance the International Linear Collider (ILC) technical design report; available at https://www.linearcollider.org/ILC/Publications/Technical-Design-Report (retrieved April, 2018).

[7] E.L. Saldin et al. *Proceedings of the 2004 FEL Conference*, 375-378.

[8] Behrens, C., et al., 2014, *Nat. Commun* 5, 3762.

[9] G. Krafft, Diagnostics for Ultrashort Bunches, *Proc. DIPAC* (1997) 48.

[10] Y. Ding, SLAC-PUB-14575

[11] Juan Serna,*et al. Journal of Optics* Volume 17, Number 10.

[12] I. Wilke, A. M. MacLeod, W. A. Gillespie, G. Berden, G. M. H. Knippels, and A. F. G. van der Meer, Phys. Rev. Lett. 88, 124801 (2002).

[13] D.J.Bradley, B.Liddy, W.E.Sleat, *Optics Communications* Volume 2, Issue 8, January 1971, Pages 391-395

[14] D. X. Wang, G. A. Krafft, and C. K. Sinclair,*Phys. Rev. E* 57, 2283.

[15] Carlsten B. E., *Proc. of the Microbunches Workshop*, AIP Conf. Proceedings No. 367, pgs. 21-35 (1995).

[16] G. Loew, O. Altenmueller, SLAC-PUB-135, 1965.

[17] S. Bettoni, P. Craievich, and M. Pedrozzi *Phys. Rev. Accel. Beams*, 19, 021304, 2016.

[18] King-Yuen Ng *Phys. Rev. D* 42, 1819, 1990.

[19] G.V. Stupakov, SLAC PUB-8683, 2000.

[20] Helmut Wiedemann, *Particle Accelerator Physics*,third edition, p673.

[21] M. Dohlus and R. Wanzenberg, *Proceedings of the CAS-CERN Accelerator School*,Vol. 3/2017.

[22] Antonella, T. *et al.*, Wake Fields in Particle Accelerators with Finite Thickness and Conductivity; available at https://www.arturostabile.com/theses.html.

[23] B.Zotter, S.Kheifets, *Impedances and Wakes in High-Energy Particle Accelerators*, World Scientific.

[24] Chao Alexander Wu, Chou Weiren,*Reviews Of Accelerator Science And Technology* , page 128.

[25] F. Lemery, P. Piot, *AIP Conference Proceedings* 1777, 070007 (2016).

[26] Abramowitz, Stegun. *Handbook of Mathematical Functions* p375.

[27] Wei Gai, *AIP Conference Proceedings* 1086, 3 (2009).

[28] C. L. Bohn and J. R. Delayen, *Phys. Rev. A* **45**, 5964 (1992).

[29] C. Behrens, *Nature Communications* **5**, Article number: 3762 (2014).

[30] M. Cornacchia and P. Emma, *Phys. Rev. ST Accel. Beams* 5, 084001 (2002).

[31] D. X. Wang, G. A. Krafft, and C. K. Sinclair,*Phys. Rev. E* 57, 2283 (1998).

[32] M. Borland, ELEGANT: A Flexible SDDS-Compliant Code for Accelerator Simulation, *Advanced Photon Source* LS-287, September 2000.

[33] Helmut Wiedemann, *Particle Accelerator Physics*, third edition, page 155.